Journal of Materials Chemistry C

Visible to near-infrared nanocrystalline organic photodetector with ultrafast photoresponse

Journal:	*Journal of Materials Chemistry C*
Manuscript ID	TC-COM-02-2022-000730.R2
Article Type:	Paper
Date Submitted by the Author:	06-May-2022
Complete List of Authors:	Xu, Wenzhan; Tsinghua University, Tsinghua-Berkeley Shenzhen Institute Gao, Yu; Tsinghua University Qian, Kun; Northern Illinois University Wang, Bingzhe; University of Macau, Institute of Applied Physics and Materials Engineering Xu, Rongguo; Peking University, Peking University Shenzhen Graduate School He, Miao; Tsinghua University Li, Tao; Northern Illinois University, Department of Chemistry and Biochemistry Xing, Guichuan; University of Macau, Institute of Applied Physics and Materials Engineering Yang, Shihe ; Peking University Shenzhen Graduate School School of Chemical Biology and Biotechnology, Wei, Guodan; Tsinghua University, Tsinghua-Berkeley Shenzhen Institute;

Visible to Near-Infrared Nanocrystalline Organic Photodetector with Ultrafast Photoresponse

Wenzhan Xu[a,b,#], Yu Gao[a,b,#], Kun Qian[c], Bingzhe Wang[d], Rongguo Xu[f], Miao He[a,b], Tao Li[c,e], Guichuan Xing[d], Shihe Yang[f] and Guodan Wei[a,b,*]

ABSTRACT: Organic photoelectron conversion devices, prized for their solution process and wide use in portable devices, have attracted intensive interests. Herein, newly developed active layer of D18:Y6 is used to fabricate organic photodetector and the device of ITO/PEDOT:PSS/D18:Y6/Phen-NaDPO/Ag shows the responsivity of 680 mA W^{-1} and the detectivity of 6.35×10^{13} Jones (1 Jones = 1 cm $Hz^{1/2}$ W^{-1}) at the wavelength of 850 nm. Additionally, this device shows a wide linear dynamic range of 120 dB, indicating a potential near-infrared region (*NIR*) detector system. Owing to minimal exciton binding energy of 37.6 meV for Y6, desirable energy offset for efficient electron-hole pair dissociation and ultrafast charge transfer of ~58 ps at the interface of D18:Y6, the obtained organic photodetector has demonstrated photoresponse time as fast as 1.8 μs upon laser light excitation without external driven voltage. More importantly, D18 shows a preferred out-of-plane orientation with strong intensities and Y6 exhibits a preferred orientation along the in-plane direction on lamellar stacking, which facilitates charge transport. This work has demonstrated significant progress on exploring D18:Y6 NIR organic device with a wide photosensitivity linearity and ultrafast photoresponse.

[a]Institute of Materials Research, Tsinghua Shenzhen International Graduate School, Tsinghua University, Shenzhen, 518055, China; E-mail: weiguodan@sz.tsinghua.edu.cn

[b] Tsinghua-Berkeley Shenzhen Institute (TBSI), Tsinghua University, Shenzhen, 518055, China

[c] Department of Chemistry and Biochemistry, Northern Illinois University, DeKalb, Illinois 60115, United States

[d] Institute of Applied Physics and Materials Engineering, University of Macau, Taipa, Macau, 999078, China

[e] X-ray Science Division and Joint Center for Energy Storage Research, Argonne National Laboratory, Lemont, Illinois 60439, United States

[f] School of Chemical Biology and Biotechnology, Shenzhen Graduate School, Peking University, Shenzhen, 518055, China

[#]W. Xu and Y. Gao are equally contributed to this work.

Introduction

Nowadays, organic semiconductor materials are of great interest due to their extended capabilities and possibilities for the next generation low-cost optoelectronic devices through facile deposition techniques.[1-3] The recently emerged high-performance photo-absorbing organic semiconductors have generated much progress in developing bulk heterojunction (BHJ) organic solar cells (OSCs) and organic photodetectors (OPDs).[4-10] Bulk heterojunction, containing blends of electron donor (D) and electron acceptor (A), offers intrinsic driving force by forming numerous D:A interfaces to dissociate optically generated excitons into free electrons and holes.[11-13] Due to the localized Frenkel or tightly bound excitons (binding energy of 0.1 to 1 eV) upon the photoexcitation in organic active layers, large energy level offsets at D/A interfaces could become energetically favorable for fast excitons dissociation and efficient charge transfer.[14, 15] However, this large energy offset increases charge carriers recombination, hindering the improvement of device performance.[16-20] Therefore, idealized D/A interfaces are essential to obtain the high and fast photosensitivity of OPDs.

To meet the great demand in a variety of applications including imaging, telecommunication, environmental monitoring and defense sensing, it is of huge necessity to develop efficient photodetectors with ultrafast photoresponse and broad response spectra ranging from visible to near-infrared light region.[21-24] Recently, organic materials have been utilized for fabricating low-cost PDs with broadband response.[25-27] Non-fullerene acceptors (NFA), owing to their tunable absorption from the ultraviolet to the near infrared region and readily tailored chemical structures that enabled finely energy level match between electron donors and electron extraction layers, have successfully captured increasing attentions and promoted device performance.[28] However, further improvement in responsivity (R) and detectivity (D^*) of broadband OPDs was hindered by their intrinsic large exciton binding energy and low charge-carrier mobilities.[29] R and D^* are two key parameters evaluating performance of PDs, which are significantly dependent on the high photocurrent density and low dark current density.

In this study, we herein select the blend of donor D18 (dithieno[3', 2':3,4;2'',3'':5,6]benzo[1,2-c][1,2,5]thiadiazole(DTBT) based polymer) and non-fullerene acceptor ((2,20-((2Z,20Z)-((12,13-bis(2ethylhexyl)-3,9-diundecyl-12,13-

dihydro-[1,2,5] thiadiazolo [3,4-e] thieno [2,"30':4',50] thieno [20,30:4,5] pyrrolo [3,2g] thieno [20,30:4,5]thieno[3,2-b] indole-2,10-diyl) bis (methanylylidene))bis(5,6-difluoro-3-oxo-2,3-dihydro-1H-indene-2,1-diylidene)) dimalononitrile) (Y6) as active layer for fabricating organic photodetector. Due to a fairly low exciton binding energy of 37.6 meV of Y6, direct exciton could be effectively dissociated without extra driving force such as D18/Y6 interface in an efficient way, contributing efficient charge separation efficiency. Additionally, a preferred orientation of D18 or Y6 film on lamellar stacking favors charge carriers transport in device, leading to effective charge collection efficiency. The obtained OPD with device architecture of ITO/PEDOT:PSS/D18:Y6/Phen-NaDPO/Ag has shown substantially low dark current density of 1.28×10^{-9} A/cm^2 at 0 V. The self-powered high responsivity of 680 mA W^{-1} and the detectivity of 6.35×10^{13} Jones (1 Jones = 1 cm Hz$^{1/2}$ W^{-1}) at the wavelength of 850 nm have been obtained due to the reduction of dark current and enhanced photocurrent generation. To note, organic photodetector exhibits a wide wavelength ranging from 300 to 1000 nm and an ultrafast photoresponse of 1.8 μs. Therefore, this work has demonstrated significant effort on exploring NIR organic device with a wide photosensitivity linearity and ultrafast photoresponse.

Results and Discussion

Atomic force microscopy (AFM) and scanning electron microscopy (SEM) of organic thin films are carried out to investigate evolution of organic layers. The nanowires seen in **Fig. 1a-c** are belonged to D18 because the crystallinity of D18 is stronger than that of Y6. It is observed that a good interpenetrating network structure in **Fig. s1**, showing a homogeneous phase separation which is due to their super miscibility between D18 and Y6.[30] The homogeneous thin film surface is also observed in AFM image (**Fig. 1a-c** and **Fig. s2**), the roughness of neat D18 and Y6 thin film is 1.47 nm and 1.36 nm, respectively, while the roughness of active layer is only 1.27 nm. Such a smooth surface facilitates direct contact with the subsequent electron extraction layer, which is benefit for electrons transport. In **Fig. 1d**, this active layer of D18:Y6 mixture exhibits broadband absorption in wavelength ranging from 380 nm to 1000 nm, which is the requisite for realizing high photocurrent responsivity density in and OPD. Since Y6 thin film has strong absorption in the wavelength of 850 nm, which is expected to contribute to high performance OPDs at the NIR.

Fig. 2a shows the device structure of ITO/PEDOT:PSS/D18:Y6/Phen-NaDPO/Ag. And corresponding energy level alignment and charge carrier transport/extraction process are illustrated in **Fig. 2b**, where Phen-NaDPO acted as the electron extraction layer, due to its deep highest occupied molecular orbital (HOMO), which efficiently blocks holes extracted from active layer to silver (Ag). The current versus voltage (*I-V*) characteristics of OPD measured in dark and under the illumination of monochromatic light at a wavelength (λ) of 780 nm (**Fig. s3**) and 850 nm (**Fig. 2c**) with various light intensity, the wavelength of 850 nm was selected due to which is located at near-infrared region and has strong absorbance intensity. It is obvious that an enhancement in current once photons are projected onto OPDs compared to dark condition, and gradually enlarged current as increased light intensity is observed, which implies charge carriers are extracted efficiently to electrodes. In order to quantitatively evaluate performance of OPDs, *R* is estimated according to the equation of

$$R = \frac{J_{ph}}{L_{light}} \quad (1)$$

where L_{light} is the light intensity. At λ = 850 nm, this organic photodetector exhibited *R* of 680, 558 and 535 mA/W at 0 V and 1209, 875 and 723 mA/W at -0.5 V for 0.0005, 0.005 and 0.05 mW/cm^2, respectively. The specific detectivity (D*) is the key figure-of-merit parameter for PD devices, which describes the detection quality of optical signals. It is depended on the device area, bandwidth, and noise current. Assuming the total noise is main dominant by the shot noise, *D** could be simplified to the shot-noise-limited specific detectivity[31, 32], which could be obtained from

$$D^* = \frac{R\sqrt{AB}}{i_n} \cong \frac{R\sqrt{AB}}{i_{sh}} = \frac{R}{\sqrt{2qJ_d}} \quad (2)$$

where i_n is the noise current, i_{sh} is the shot noise current and q is the absolute value of electron charge (q = 1.6 x 10^{-19} C) and the corresponding *D** are 1.83, 1.58 and 1.34 ×10^{13} Jones at -0.5 V for 0.0005, 0.005 and 0.05 mW/cm^2, respectively (**Table 1**). These values are higher than those of reported OPDs based on Y6 non-fullerene acceptor (**Table s2**),[28, 33, 34] and compare to or even higher than commercial inorganic materials or perovskite PDs in some cases (**Table 2**).[24, 35] To obtain quantitatively *R* in the spectral range of 300 nm to 1000 nm, the *R* of OPDs verse wavelength are shown in **Fig. 2d**,

$$R = EQE \times \frac{q\lambda}{hc} \quad (4)$$

where h is Plank constant, c is the speed of light. The calculated Rs from EQE are few hundreds mA/W and D^* is over 10^{13} Jones in the visible region. Specifically, it exhibits the R of 556 mA/W and the D^* of 5.42×10^{13} Jones at the wavelength of 850 nm, which are consistent with those measured from the light intensity of 0.005 mW/cm^2.

On the other hand, the D^* value is accurately detected by measuring the noise current, which can be calculated as follows[36]

$$D^* = \frac{\sqrt{A}}{NEP} = \frac{R\sqrt{A}}{\sqrt{i_{noise}}} \quad (3)$$

where NEP and i_{noise} are the noise equivalent power and the noise current, respectively. To accurately detected the D^* values, the noise spectral density of devices was measured (**Figure 2e)**. According to the Equation (3), taking the noise spectral density at 10 Hz with light intensity of 0.005 mW/cm^2, the D^* values of the OPDs were calculated to be 5.58×10^{10} Jones and 4.73×10^{10} *Jones* at 0 V and -0.5 V, respectively. When the noise spectral density increased to 10^5 Hz, the D^* values of the OPDs were calculated to be 1.22×10^{13} Jones and 4.77×10^{12} *Jones* at 0 V and -0.5 V, respectively (**Table s1**).

Frequency response of OPD at 900 nm was characterized from 1 Hz to 10^5 Hz in **Fig. 2f**, it was obvious that the −3 dB cutoff frequency of devices based on D18:Y6 was determined to be 6.5×10^4 Hz, which predicted a fast photo response process.[37, 38]The response time of PD, a direct indication reflecting PD performance, is also investigated. Rise time and decay time are defined as the interval in which current increased from 10% to 90%, and transition from 90% down to 10% of the peak current,[24] respectively. As shown in **Fig. 3a**, it is measured that rise time is 1.8 μs and decay time is as small as 2.2 μs, indicating this device exhibits an ultrafast response time, which is inherently related to their interpenetrating interfaces in the bulk D18 and Y6 mixture and idealized device architecture. The linear dynamic region (*LDR*) or photosensitivity linearity (typically quoted in dB) is estimated according to the equation of

$$LDR = 20\log\left(\frac{J_{max}}{J_{min}}\right) \quad (5)$$

where J_{max} and J_{min} are the maximum and minimum of the linear part of detectable light intensity at a given wavelength, respectively. The photocurrent versus the incident light

intensity of OPD is shown in **Fig. 3b**. In the region of linear photosensitivity for OPD, J_{max} and J_{min} are the photocurrent density measured at the light intensity of 10 mW cm^{-2} and 4.0 × 10^{-6} mW cm^{-2}, respectively. Therefore, it is calculated that the OPD possesses 120 dB LDR, which is comparable to inorganic photodetectors.[39]

To explore the charge carrier extraction and recombination dynamics in device, transient photocurrent (TPC) and transient photovoltage (TPV) of devices are measured.[40-43] As shown in **Fig. 3c**, the curve tends to be linear at the first stage due to most of high mobility charge carriers are generated and extracted within a relatively short time, and then followed by a long tail which is originated from charge carriers being trapped and detraped.[44] This device exhibits short charge carrier extraction time of 0.58 μs, suggests a fast charge carrier extraction. In **Fig. 3d**, TPV is fitted by mono-exponential decay with $\delta V = V_M e^{(-\tau/T)}$, where V_M is a constant that fits to the peak, τ is the time and T is the decay time constant. Encouragely, long charge carrier lifetime of 133 μs from TPV is achieved. The fast charge carrier extraction process suggests that photogenerated charge carriers are effectively extracted to respective electrodes, and long charge carrier lifetime indicates that charge carrier recombination is significantly reduced which is conducive to high current density, therefore high device performance.

In order to analysis devices with active layer of D18:Y6 exhibit high efficiency as OSC and high responsivity and detectivity as OPD simultaneously, firstly the exciton binding energy of Y6 is calculated. As shown in **Fig. 4a**, the temperature dependent photoluminescence (PL) of Y6 thin film shows that the PL intensity decreased as temperature increased from 85 to 325 K due to thermal quenching. It is notice that, with the increased temperature, a 70 nm blue shift is observed. **Fig. 4b** shows the temperature dependent integrated PL intensity curve. The exciton binding energy (E_b) can be calculated by the following equation of [45, 46]

$$I(T) = \frac{I_0}{1 + A\, exp(-\frac{E_b}{k_B T})} \quad (6)$$

where A is a proportional constant, $I(T)$ and I_0 are the integrated PL intensity at temperature T and 0 K, respectively, and k_B is the Boltzmann constant. In order to clearly understand the state and transfer process of Frenkel excitons, a simple schematic structure is depicted in **Fig. 4c.** Frenkel excitons (electron-hole bounded pair) generate after light illumination

to absorbing-photo materials, which are commonly not able to dissociate into free electron and hole until being transferred into interface of D:A due to large binding energy of about few hundred meV (**Table s3**). Here, it is calculated that Y6 has the low E_b of 37.6 meV, which is likely due to strong polarization effects of charge carriers.[47] Such exciton binding energy is one of the smallest Frenkel excitons binding energy compare with reported work (**Table s3**), even a bit lower than 40 meV for reported 4TIC,[48, 49] a commonly used NFA in organic devices.[50] Such small exciton binding energy which means excitons generated in Y6 could be directly dissociated into free electron and hole under extent temperature.

Femtosecond transient absorption spectroscopy (TAS) is employed to further explore the ultrafast charge transfer process and recombination mechanism at D18:Y6 film.[51-53] **Fig. 4d** and **Fig. s4** show representative TA spectra (ΔA) of organic thin layer at selected probe delay times (the TA was performed under 360 nm excitation at 1 KHz, 100 fs, around 1 μJ/cm^2/pulse). Once photoexcitation excited by pump laser from the ground state to excited state and probe beam detects the absorption, a new component due to excited state absorption appears, as well as a reduction in the ground state absorption depleted by the pump pulse, which is called ground state bleaching. It shows three notable photoinduced photobleaching (PB) signals (negative signals at 550 nm (PB1, n=1), 590 nm (PB2, n=2), and 850 nm (PB3, n=3)), these negative bands are due to the excited state absorption of D18 and Y6 in the blend film, which are also confirmed in the pristine D18 film and pristine Y6 film (**Fig. s5**). The PB positions of these transitions are in good consistent with the steady-state absorption peaks (**Fig. 1d**). It is also found that the absorption band at ~950 nm, which is absent in pristine D18 or Y6 film, is due to the absorption of polarons in charge separated states.

Regarding the temporal characteristics of charge carrier transfer, we have compared the kinetic decay-associated spectrum (DAS) process at 850 nm for blend layer (**Fig. 4e**), fitting results yield three kinetic components of 0.86 ps, 58 ps and 1258 ps in **Table s4**. It indicats that Y6 singlet exciton decay and polaron is rapidly generated with a time constant of 0.86 ps. Excitons migrate and reach the donor-acceptor interface can be separated into the electron on the acceptor and the hole on the donor, where 58 ps is the charge (exction) transfer time [54] at the D18/Y6 interfaces. The ultrafast charge transfer time of 58 ps is inheriently beneficial for the enhanced electron-hole pair separation, resulting in fast

charge carrier extraction time conducted by TPC for the efficient D18:Y6 device (**Fig. 3c**) and fast rise time of 1.8 μs for the high performance D18:Y6 OPD (**Fig. 3a**). Also, exciton geminate recombination to the ground state occurs, which shows a recombination time constant of 1258 ps.

Steady-state photoluminescence (PL) and Time-resolved photoluminescence (TRPL) spectra of the corresponding films are conducted to further study the charge carrier dynamic processes (charge separation, transport and recombination).[55] As shown in Fig. s5, the D18 and Y6 film on ITO glass exhibits a pronounced PL emission peak around 702 nm and 920 nm, respectively, whereas efficient PL quenching is observed in the D18:Y6 composite film. This indicates efficient charge transfer between D18 and Y6 in the composite. This promoted charge transfer D18:Y6 mixture is further evidenced by the TRPL results (**Fig. 4f** and **Fig. s6)**, the excitation wavelength is 400 nm for all thin films. The emission lifetime of neat D18 (monitored by 630 nm) and Y6 (monitored by 780 nm due to measurement equipment limitation, 850 nm should be the optimal one) thin film is 84 ps and 271 ps, respectively. However, the remarkedly decreased emission lifetime of blend thin films, which are 32 ps and 36 ps for emission of 630 and 780 nm, respectively, can be observed. The shortened lifetime may be due to efficient exciton dissociation or charge transfer at D18/Y6 interfaces, as a result, which is contribute to devices achieving fast photoresponse (~ 1.8 μs).

The intrinsic molecular packing of D18, Y6 and D18:Y6 was characterized with grazing-incidence small-angle X-ray scattering (GISAXS) (**Fig. 5**). GISAXS is a powerful tool to distinguish the arrangements of polymers at the nanoscale.[56] In this study, the characteristic length is around 1.9 nm as the effective q value is between 0.07~1 $Å^{-1}$ in the out-of-plane (OOP) direction and 0.07~0.8 $Å^{-1}$ in the in-plane (IP) direction. As can be seen in **Fig. 5a-c**, the scattering pattern of neat D18 film mainly includes a triangle-like scattering area near the beam-stop and a bright round scattering spot on the top. A line-cut along the IP direction reveals two peaks at q=0.29 $Å^{-1}$ and q=0.55 $Å^{-1}$, which are assigned to the diffraction peaks of (100) and (002), respectively.[30] The (100) peak is associated with the lamellar stacking based on previous report.[30] In our observation, the lamellar diffraction peak has a preferred OOP orientation which has strong intensities in the OOP direction, while low intensities distributed as a weak but observable scattering arc. The line-cut along the OOP direction

suggests that the bright scattering spot centered at q_z= 0.34 Å^{-1}, corresponding to a characteristic distance of ~1.85 nm. Such a distance is also consistent with the spacing between stacked D18 lamellae by previous molecular dynamic (MD) simulation.[30] The neat Y6 film displays a needle-like scattering pattern in the center. The wider scattering shape around the beam-stop indicates that there are large aggregates in the film, which could be verified by that the intensity increased dramatically with the decrease of q in the OOP direction (**Fig. 5d-e**). Besides, the line-cut analysis also suggests that there is no lamellar peak (100) appeared along the OOP direction, while it was clearly observed in the IP direction. Such a feature suggests the Y6 film still has a preferred orientation along the IP direction on lamellar stacking, although the overall stacking structure is weak. Beside the lamellar peak at q=0.29 Å^{-1}, another peak at q=0.41 Å^{-1} is also observed, which is originated from the (001) diffraction, implying the backbone ordering of Y6 that facilities the intermolecular electron transport.[57] Interestingly, after mixing Y6 with D18, the intrinsic OOP orientation of D18 totally disappeared. At the same time, the scattering intensity of (100) were concentrated between q_z=0~0.2 Å^{-1}. And also, the aggregation in D18:Y6 film is obviously less than the pure Y6 film. The line-cut profile along the IP presents clear diffraction peaks from both D18 and Y6, which reveals that blending does not impact their own packing feature along the IP direction. The preferred orientation could be measured by the scattering intensity as a function of polar angle (χ) with respect to the q-vector of the (100) planes.[58] **Fig. s7** compares the χ scattering profiles of D18, Y6 and D18:Y6. It shows that the scattering intensity is higher at smaller χ for D18, while inverse for D18:Y6. A previous study attributed the excess scattering intensity at smaller χ to oriented edge-on, and excess scattering intensity at larger χ as due to oriented face-on. Therefore, D18 has edge-on orientation and Y6 has a face-on orientation (**Fig. s8**).

Conclusion

In summary, we fabricate fast response, high responsivity and detectivity organic photodetector with D18:Y6 active layer herein. Small Frenkel exciton binding energy of 37.6 meV in Y6 ensures exciton can be efficiently dissociated, which promotes a high photocurrent density for device. The matched energy level alignment in thin films acerates charge carriers transport and extraction for high device performance along with suppressed charge carrier recombination. TPC and TPV measurements show a very short charge

carrier extraction time of 0.58 μs and a relative long charge carrier lifetime of 133 μs, respectively. TAS and TRPL results further confirm that efficient exciton dissociation or ultrafast charge transfer at D18/Y6 interfaces occurs. GISAXS results exhibit preferred orientation along the OOP or IP direction on lamellar stacking in organic film help the intermolecular electron transport from backbone ordering of Y6. As a result, the fabricated organic photodetector achieves the responsivity of 680 mA W^{-1} and the detectivity of 6.35 × 10^{13} Jones under zero bias at the wavelength of 850 nm, respectively, operated at room temperature. In addition, it is the first time that this type of device exhibits a high detectivity and responsivity simultaneously to our best knowledge.

Experimental section

Materials: D18 and Y6 were purchased from One Material; Chloroform (CF, 99.8%) was purchased from Sigma Aldrich; Ethanol was purchased from Alfa Aesar; PEDOT:PSS (Clevios P VP Al 4083) was purchased from Heraeus; Phen-NaDPO was purchased from Puri Material Technology Co. Ltd. All materials and reagents were used as received without further purification.

Fabrication of photovoltaic devices: Ultrasound cleaning of ITO-coated glass substrates with ethanol, acetone solution, deionized water for 20 minutes, respectively, then drying the substrates in dry oven overnight. After that, the BHJ device with structure of ITO/PEDOT:PSS/D18:Y6/Phen-NaDPO/Ag is fabricated. Fristly, ~ 40 nm PEDOT:PSS layer is spin-coated onto pre-cleaned and UV-Ozone treated ITO-coated glass substrates at 4000 round per minutes (RPM) for 30 seconds (s), followed with thermal annealing at 150 °C for 15 minutes (min) on the hotplate. Then the substrates are transferred into N_2-golvebox, ~90 nm D18:Y6 active layer is spin-coated on top of PEDOT:PSS layer from D18:Y6 (1:1.6 by weight) chloroform solution, followed with solvent annealing for 50 μL CF in covered petri dish for 5 min. After that, 5 nm Phen-NaDPO layer is spin-coated on top of D18:Y6 layer from Phen-NADPO solution (0.5 mg/mL in Ethanol), Finally, ~100 nm of Ag is sequentially thermally evaporated by a shadow mask under a pressure of 2 x 10^{-6} mbar. The effective device area is measured to be 0.06 cm^2.

Characterization of organic thin films: UV-vis-NIR absorption and photoluminescence (PL) spectra of thin films were recorded on a HP 8453 spectrophotometer and FLS920 Spectro fluorimeter (Edinburgh Instruments), respectively. Scanning electron microscope

(SEM) images were obtained by using a field emission scanning electron microscope (JEOL-7401). Thicknesses of thin films were measured by Dektak 150 surface profilometer. AFM-based measurement was performed on Asylum Research Cypher AFM with/without the built-in LED sheds light on the sample from the top. The broadband fs-TA measurements were carried out on a Heliospump-probe system (Ultrafast Systems LLC) coupled with an amplified femtosecond laser system (Coherent, 35 fs, 1 kHz, 800 nm). The probe pulses (from 380 to 800 nm) were generated by focusing a small portion (around 10 μJ) of the fundamental 800-nm laser pulses into a 1-mm CaF_2. The 365nm pump pulses were generated from an optical parametric amplifier (TOPAS-800-fs). TA curves as a function of delay time were fitted to a biexponential decay functions of $y = y_0 + A_1 e^{-t/\tau_1} + A_2 e^{-t/\tau_2} + A_3 e^{-t/\tau_3}$. GISAXS patterns were measured using 18 keV X-rays at beamline 12-ID-C at the Advanced Photon Source (APS) of Argonne National Laboratory. An area detector, MarCCD 165 was used to detect the scattered photons. The samples were thin polymer films coated on ITO glasses. The incidence angle is 0.09° and the sample to detector distance is ~2 m.

Characterization of photovoltaic devices: The cells were connected to a digital oscilloscope (Tektronix DPO-3054) and the input impedance of the oscilloscope was set to 100 MΩ and 50 Ω, respectively, for monitoring the charge density decay. The transient photovoltage was measured under 0.3 sun background illumination. An attenuated laser pulse (500 nm) was used as a small perturbation to the background illumination on the device. The laser-pulse-induced photovoltage variation was smaller than 5% of the V_{OC} produced by the background illumination. The transient photocurrent was measured by applying 500 nm laser pulses with a pulse width of 120 fs and a low pulse energy to short circuit devices in the dark. The laser pulses were generated from an optical parametric amplifier (TOPAS-Prime) pumped by a mode-locked Ti:sapphire oscillator seeded regenerative amplifier with a pulse energy of 1.3 mJ at 800 nm and a repetition rate of 1 kHz (Spectra Physics Spitfire Ace). All *I-V* and *current-time* curves measurements were carried out with a home-build system at room temperature which consisted of the optical and electrical parts. The optical part includes SC-PRO and AOTF-PRO produced by OYSL and can produce 430-2000 nm light which provide the illumination needed by

photodetectors. The electrical part consists of probe and Keithley 2600B and can detect the photodetectors' current. The fast current-time curves were measured using the semiconductor analyzing system and digital oscilloscope at room temperature (Keithley 4200A-SCS, USA, LakeShore, USA, Tektronix DPO-3054). Measurement of noise current and calculation of *NEP* and *D**: the photoconductive device was placed inside an electrically shielded and optically sealed probe station and connected in series with a Stanford Research SR830 lock-in amplifier. Batteries were used to bias the device for the measurement of the noise current to minimize noise components from the bias source. Through the choice of integration time, lock-in amplifier reported a noise current in $A/Hz^{1/2}$. The noise current divided by the responsivity under the same experimental conditions (applied bias and electronic bandwidth) yielded the noise equivalent power (*NEP*). To validate the *NEP* obtained using this technique, the identical procedure was carried out using a commercial Si detector with known NEP.

Supporting Information

The Supporting Information is available from the Wiley Online Library or from the author.

Acknowledgements

This project was supported by National Natural Science Foundation of China (Grant Number: 03012800001). This work was financially also supported by Shenzhen Science and Technology Innovation Committee (JCYJ20190809172615277), Guangdong Basic and Applied Basic Research Foundation (2020A1515111065). This research used resources of the Advanced Photon Source, a U.S. Department of Energy (DOE) Office of Science User Facility operated for the DOE Office of Science by Argonne National Laboratory under Contract No. DE-AC02-06CH11357.

Conflict of Interest

The authors declare no competing financial interest.

Keywords

Organic photodetectors, low exciton binding energy, high responsivity, ultrafast photoresponse

REFERENCES

1 Q. Liu, Y. Jiang, K. Jin, J. Qin, J. Xu, W. Li, J. Xiong, J. Liu, Z. Xiao, K. Sun, S. Yang, X. Zhang and L. Ding, *Sci. Bull.*, 2020, **65**, 272-275.

2 D. Yang and D. Ma, *Adv. Opt. Mater.*, 2019, **7**.

3 C. Wang, B. Fu, X. Zhang, R. Li, H. Dong and W. Hu, *ACS Central Science*, 2020, **6**, 636-652.

4 Y. Lin, Y. Firdaus, M. I. Nugraha, F. Liu, S. Karuthedath, A. H. Emwas, W. Zhang, A. Seitkhan, M. Neophytou and H. Faber, *Advanced Science*, 2020, **7**, 1903419.

5 M. Cui, D. Li, X. Du, N. Li, Q. Rong, N. Li, L. Shui, G. Zhou, X. Wang and C. J. Brabec, *Advanced Materials*, 2020, **32**, 2002973.

6 Y. Wang, Y. Wang, L. Zhu, H. Liu, J. Fang, X. Guo, F. Liu, Z. Tang, M. Zhang and Y. Li, *Energy & Environmental Science*, 2020, **13**, 1309-1317.

7 X. Liu, Y. Lin, Y. Liao, J. Wu and Y. Zheng, *Journal of Materials Chemistry C*, 2018, **6**, 3499-3513.

8 W. Li, Y. Xu, X. Meng, Z. Xiao, R. Li, L. Jiang, L. Cui, M. Zheng, C. Liu and L. Ding, *Advanced Functional Materials*, 2019, **29**, 1808948.

9 Q. Li, Y. Guo and Y. Liu, *Chemistry of Materials*, 2019, **31**, 6359-6379.

10 J. Liu, Y. Wang, H. Wen, Q. Bao, L. Shen and L. Ding, *Solar RRL*, 2020, **4**.

11 J.-S. Wu, S.-W. Cheng, Y.-J. Cheng and C.-S. Hsu, *Chemical Society Reviews*, 2015, **44**, 1113-1154.

12 C. Deibel, T. Strobel and V. Dyakonov, *Advanced materials*, 2010, **22**, 4097-4111.

13 D. Qian, Z. Zheng, H. Yao, W. Tress, T. R. Hopper, S. Chen, S. Li, J. Liu, S. Chen and J. Zhang, *Nature materials*, 2018, **17**, 703-709.

14 K. H. Hendriks, A. S. Wijpkema, J. J. van Franeker, M. M. Wienk and R. A. Janssen, *Journal of the American Chemical Society*, 2016, **138**, 10026-10031.

15 L. Zhu, Y. Yi and Z. Wei, *The Journal of Physical Chemistry C*, 2018, **122**, 22309-22316.

16 B. P. Rand, D. P. Burk and S. R. Forrest, *Physical Review B*, 2007, **75**, 115327.

17 M. Azzouzi, T. Kirchartz and J. Nelson, *Trends in Chemistry*, 2019, **1**, 49-62.

18 D. Di Nuzzo, G. J. A. Wetzelaer, R. K. Bouwer, V. S. Gevaerts, S. C. Meskers, J. C. Hummelen, P. W. Blom and R. A. Janssen, *Advanced Energy Materials*, 2013, **3**, 85-94.

19 F. Eisner, G. Foot, J. Yan, M. Azzouzi, D. G. Georgiadou, W. Y. Sit, Y. Firdaus, G. Zhang, Y.-H. Lin, H.-L. Yip, T. D. Anthopoulos and J. Nelson, *Advanced Materials*, 2021, **n/a**, 2104654.

20 S.-J. He, D.-K. Wang, N. Jiang and Z.-H. Lu, *The Journal of Physical Chemistry C*, 2016, **120**, 21325-21329.

21 X. Gong, M. Tong, Y. Xia, W. Cai, J. S. Moon, Y. Cao, G. Yu, C.-L. Shieh, B. Nilsson and A. J. Heeger, *Science*, 2009, **325**, 1665-1667.

22 D. Yang, X. Zhou, Y. Wang, A. Vadim, S. M. Alshehri, T. Ahamad and D. Ma, *Journal of Materials Chemistry C*, 2016, **4**, 2160-2164.

23 L. Shen, Y. Lin, C. Bao, Y. Bai, Y. Deng, M. Wang, T. Li, Y. Lu, A. Gruverman and W. Li, *Materials Horizons*, 2017, **4**, 242-248.

24 W. Xu, Y. Guo, X. Zhang, L. Zheng, T. Zhu, D. Zhao, W. Hu and X. Gong, *Advanced Functional Materials*, 2018, **28**, 1705541.

25 L. Zheng, T. Zhu, W. Xu, L. Liu, J. Zheng, X. Gong and F. Wudl, *Journal of Materials Chemistry C*, 2018, **6**, 3634-3641.

26 F.-C. Chen, S.-C. Chien and G.-L. Cious, *Applied Physics Letters*, 2010, **97**, 195.

27 Z. Zhao, C. Xu, L. Niu, X. Zhang and F. Zhang, 2020, **14**, 2000262.

28 Z. Zhong, F. Peng, Z. Huang, L. Ying, G. Yu, F. Huang and Y. Cao, *ACS Appl Mater Interfaces*, 2020, **12**, 45092-45100.

29 Y. Yu, B. Luszczynska and M. Z. Szymanski, *Semiconductor Science and Technology*, 2020, **35**, 104002.

30 Z. Wang, Z. Peng, Z. Xiao, D. Seyitliyev, K. Gundogdu, L. Ding and H. Ade, *Adv Mater*, 2020, **32**, e2005386.
31 Y. Chen, Y. Zheng, Y. Jiang, H. Fan and X. Zhu, *J. Am. Chem. Soc.*, 2021, **143**, 4281-4289.
32 J. Liu, M. Gao, J. Kim, Z. Zhou, D. S. Chung, H. Yin and L. Ye, *Mater. Today*, 2021, **51**, 475-503.
33 B. Xie, R. Xie, K. Zhang, Q. Yin, Z. Hu, G. Yu, F. Huang and Y. Cao, *Nature Communications*, 2020, **11**, 2871.
34 Z. Zhao, J. Wang, C. Xu, K. Yang, F. Zhao, K. Wang, X. Zhang and F. Zhang, *The Journal of Physical Chemistry Letters*, 2020, **11**, 366-373.
35 L. Dou, Y. M. Yang, J. You, Z. Hong, W. H. Chang, G. Li and Y. Yang, *Nat. Commun.*, 2014, **5**, 5404.
36 P. C. Y. Chow and T. Someya, *Adv. Mater.*, 2020, **32**, 1902045.
37 C. Bao, Z. Chen, Y. Fang, H. Wei, Y. Deng, X. Xiao, L. Li and J. Huang, 2017, **29**, 1703209.
38 J. Li, G. Zhang, Z. Zhang, J. Li, Z. Uddin, Y. Zheng, Y. Shao, Y. Yuan, B. J. A. A. M. Yang and Interfaces, 2021.
39 G. Konstantatos, I. Howard, A. Fischer, S. Hoogland, J. Clifford, E. Klem, L. Levina and E. H. Sargent, *Nature*, 2006, **442**, 180-183.
40 J. Seifter, Y. Sun and A. J. Heeger, *Advanced Materials*, 2014, **26**, 2486-2493.
41 J. Seifter, Y. Sun, H. Choi, B. H. Lee, T. L. Nguyen, H. Y. Woo and A. J. Heeger, *Advanced Materials*, 2015, **27**, 4989-4996.
42 F. Gao, Z. Li, J. Wang, A. Rao, I. A. Howard, A. Abrusci, S. Massip, C. R. McNeill and N. C. Greenham, *Acs Nano*, 2014, **8**, 3213-3221.
43 Y. Shao, Z. Xiao, C. Bi, Y. Yuan and J. Huang, *Nature communications*, 2014, **5**, 5784.
44 W. Xu, L. Zheng, X. Zhang, Y. Cao, T. Meng, D. Wu, L. Liu, W. Hu and X. Gong, *Advanced Energy Materials*, 2018, DOI: 10.1002/aenm.201703178, 1703178.
45 P. Liu, Y. Liu, S. Zhang, J. Li, C. Wang, C. Zhao, P. Nie, Y. Dong, X. Zhang, S. Zhao and G. Wei, *Adv. Opt. Mater.*, 2020, **8**.
46 B. Yang, L. Yin, G. Niu, J. H. Yuan, K. H. Xue, Z. Tan, X. S. Miao, M. Niu, X. Du, H. Song, E. Lifshitz and J. Tang, *Advanced Materials*, 2019, **31**, 1904711.
47 L. Zhu, J. Zhang, Y. Guo, C. Yang, Y. Yi and Z. Wei, *Angew Chem Int Ed Engl*, 2021, **60**, 15348-15353.
48 L. Perdigón-Toro, H. Zhang, A. Markina, J. Yuan, S. M. Hosseini, C. M. Wolff, G. Zuo, M. Stolterfoht, Y. Zou and F. Gao, *Advanced Materials*, 2020, **32**, 1906763.
49 L. Zhu, Z. Tu, Y. Yi and Z. Wei, *J Phys Chem Lett*, 2019, **10**, 4888-4894.
50 X. Shi, L. Zuo, S. B. Jo, K. Gao, F. Lin, F. Liu and A. K. Y. Jen, *Chemistry of Materials*, 2017, **29**, 8369-8376.
51 X. Yi, B. Gautam, I. Constantinou, Y. Cheng, Z. Peng, E. Klump, X. Ba, C. H. Y. Ho, C. Dong, S. R. Marder, J. R. Reynolds, S.-W. Tsang, H. Ade and F. So, 2018, **28**, 1802702.
52 H. Gu, C. Liang, Y. Xia, Q. Wei, T. Liu, Y. Yang, W. Hui, H. Chen, T. Niu, L. Chao, Z. Wu, X. Xie, J. Qiu, G. Shao, X. Gao, G. Xing, Y. Chen and W. Huang, *Nano Energy*, 2019, **65**.
53 X. Song, L. Hou, R. Guo, Q. Wei, L. Yang, X. Jiang, S. Tu, A. Zhang, Z. Kan, W. Tang, G. Xing and P. Müller-Buschbaum, *ACS Applied Materials & Interfaces*, 2021, **13**, 2961-2970.
54 W. Xu, Y. Gao, W. Ming, F. He, J. Li, X. H. Zhu, F. Kang, J. Li and G. Wei, *Adv Mater*, 2020, DOI: 10.1002/adma.202003965, e2003965.
55 L. Zhan, S. Li, T.-K. Lau, Y. Cui, X. Lu, M. Shi, C.-Z. Li, H. Li, J. Hou and H. Chen, *Energy & Environmental Science*, 2020, **13**, 635-645.
56 D. Qiu, M. A. Adil, K. Lu and Z. Wei, *Front Chem*, 2020, **8**, 603134.

57 J. Yuan, Y. Zhang, L. Zhou, G. Zhang, H.-L. Yip, T.-K. Lau, X. Lu, C. Zhu, H. Peng, P. A. Johnson, M. Leclerc, Y. Cao, J. Ulanski, Y. Li and Y. Zou, *Joule*, 2019, **3**, 1140-1151.

58 K. G. Y. Danvers E. Johnston, Htay Hlaing, Xinhui Lu, Benjamin M. Ocko, and Charles T. Black, *ACS nano*, 2014, **8**, 243-249.

59 X. Liu, H. Wang, T. Yang, W. Zhang and X. Gong, *ACS Applied Materials & Interfaces*, 2012, **4**, 3701-3705.

60 A. Armin, M. Hambsch, I. K. Kim, P. L. Burn, P. Meredith and E. B. Namdas, *Laser & Photonics Reviews*, 2014, **8**, 924-932.

61 I. K. Kim, B. N. Pal, M. Ullah, P. L. Burn, S.-C. Lo, P. Meredith and E. B. Namdas, *Advanced Optical Materials*, 2015, **3**, 50-56.

62 X. Zhou, D. Yang and D. Ma, *Advanced Optical Materials*, 2015, **3**, 1570-1576.

63 J. Huang, J. Lee, J. Vollbrecht, V. V. Brus, A. L. Dixon, D. X. Cao, Z. Zhu, Z. Du, H. Wang, K. Cho, G. C. Bazan and T.-Q. Nguyen, *Advanced Materials*, 2020, **32**, 1906027.

Table 1 Device performance parameters of OPD measured under the illumination of monochromatic light at a wavelength (λ) of 850 nm) with light intensity of 0.0005, 0.005 and 0.05 mW/cm^2.

850 nm (mW/cm^2)	J_{ph} (0 V) (A/cm^2)	J_{ph}(-0.5 V) (A/cm^2)	J_{dark} (0 V) (A/cm^2)	J_{dark} (-0.5 V) (A/cm^2)	R (0 V) (mA/W)	R (-0.5 V) (mA/W)	D^* (0 V) (10^{13} Jones)	D^* (-0.5 V) (10^{13} Jones)
0.0005	3.10×10^{-6}	5.51×10^{-6}	1.28×10^{-9}	4.87×10^{-8}	680	1209	6.35	1.83
0.005	2.78×10^{-5}	4.36×10^{-5}	1.28×10^{-9}	4.87×10^{-8}	558	875	5.48	1.58
0.05	2.67×10^{-4}	3.61×10^{-4}	1.28×10^{-9}	4.87×10^{-8}	535	723	4.63	1.34

Table 2 A summary of the detail performance parameters of various photodetectors

Catgory	Active layer	Spectra (nm)	J_{dark} (A cm^{-2})	R (mA W^{-1})	D^* (Jones)	Ref.
Organic Materials	P3HT:PCBM	350-750	1 x 10^{-9}(-0.5 V)	320(-0.5 V)	1 x 10^{13}(-0.5 V)	[59]
	PCDTBT:$PC_{70}BM$	300-750	1 x 10^{-9}(-1 V)	N/A	2 x 10^{13}(-1 V)	[60]
	p-DTS($FBTTh_2$)$_2$:$PC_{71}BM$	300-800	1 x 10^{-10}(-0.5 V)	400 (-0.5 V)	2 x 10^{12}(-0.5 V)	[61]
	PDPP3T:$PC_{71}BM$	300-1000	6.4 x 10^{-10}(-0.5 V)	200 (-1)	1.5 x 10^{13}(-0.5 V)	[62]
	PTB7-Th:CO1-4Cl	400-1100	7 x 10^{-9}(-2 V)	450 (-0.1 V)	3.3 x 10^{13}(-0.1 V)	[63]
Inorganic Materials	Si	320-1100	1.7 x 10^{-9}(-0.01 V)	500 (-0.01 V)	2.6 x 10^{13}(-0.01 V)	Commerical
	InGaAs	500-1700	2 x 10^{-7}(-1 V)	1000 (-1 V)	5 x 10^{12}(-1 V)	Commerical
Perovskites	$CH_3NH_3PbI_{3-x}Cl_x$	350-800	1 x 10^{-9}(-0.1 V)	N/A	8 x 10^{13}(-0.1 V)	[35]
	$CH_3NH_3PbI_3$/NDI-DPP	380-1300	1 x 10^{-8}(-0.5 V)	400@550nm	6 x 10^{12}(-0.5 V)	[24]
				150@1064nm	2 x 10^{12}(-0.5 V)	
	D18:Y6	300-1200	1.28 x 10^{-9}(0 V)	680(0 V)	6.35 x 10^{13}(0 V)	**This work**
		300-1200	4.87 x 10^{-8}(-0.5V)	1209 (-0.5V)	1.83 x 10^{13}(-0.5 V)	

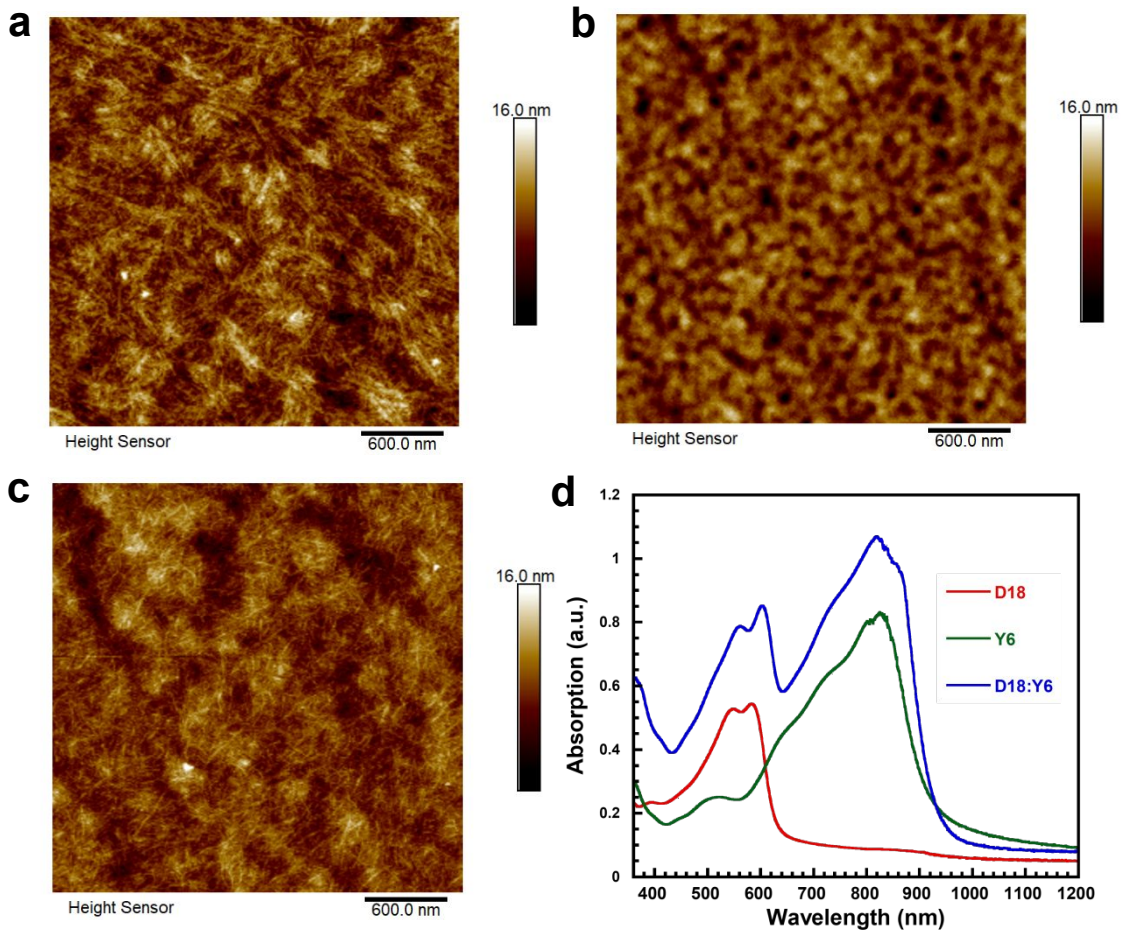

Fig. 1. (a) The 2D view AFM image of D18 thin film. (b) The 2D view AFM image of Y6 thin film. (c) The 2D view AFM image of D18:Y6 thin film. (d) Absorption spectra of D18, Y6 and D18:Y6 thin film.

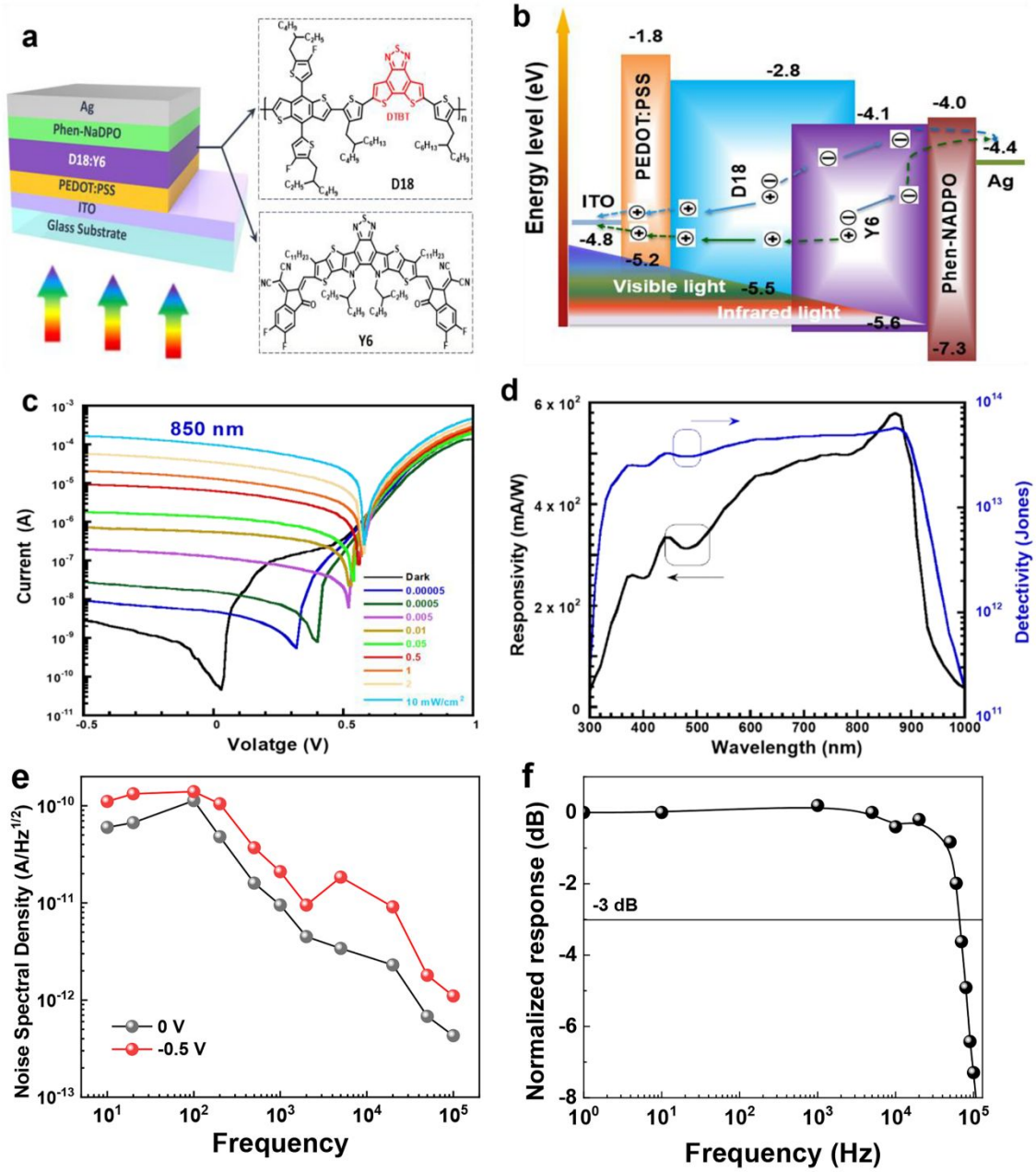

Fig. 2. (**a**) The device structure, the molecular structure of D18 and Y6. (**b**) The corresponding energy level alignment of various thin films and charge carriers transport/extraction process. (**c**) The I-V curves of OPD dependence at 850 nm on power density. (**d**) Responsivity and detectivity of OPD dependence on wavelength (Both the responsivity and detectivity were carried out with an applied voltage of 0V). (**e**) Noise spectral density of OPD at different bias. (**f**) Frequency response of OPD (0 V) at 900 nm.

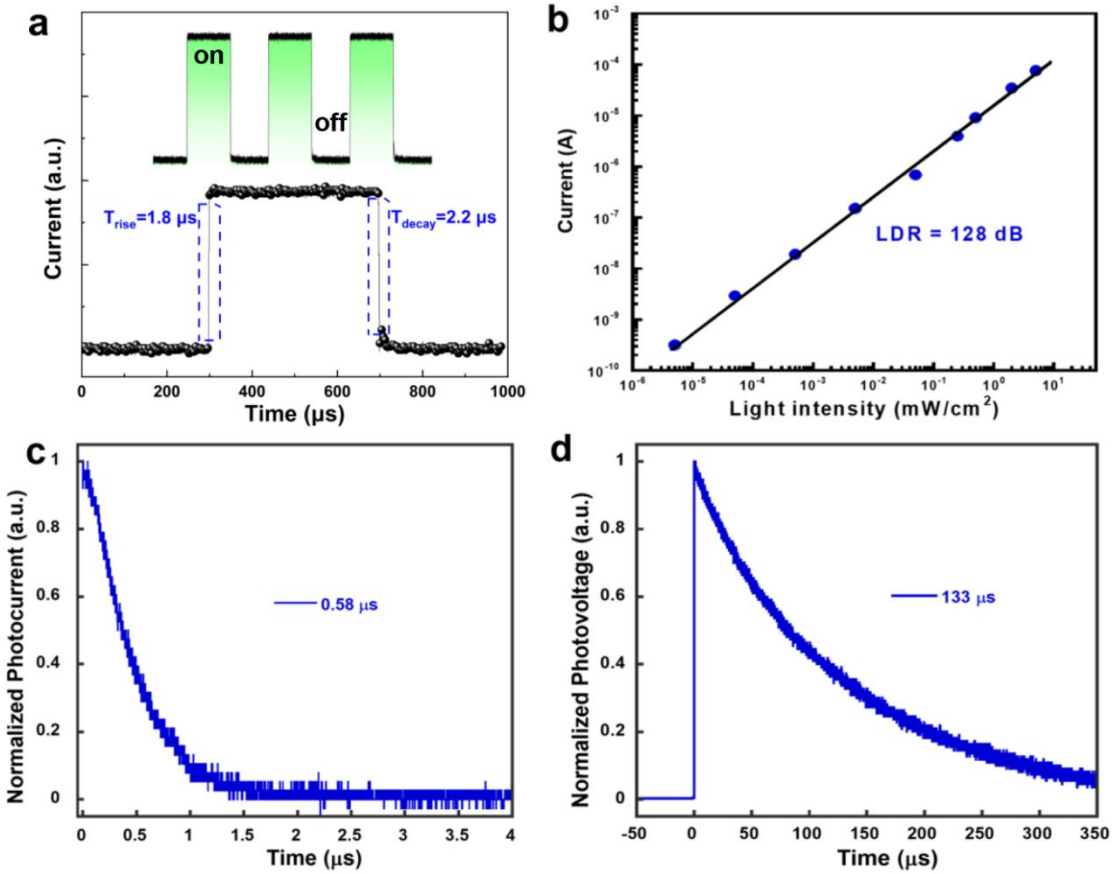

Fig. 3. (**a**) The response time (rise and decay) of OPD at wavelength of 850 nm. Inset: The current-time curve of corresponding OPD at 850 nm. (**b**) The linear dynamic region (LDR) or photosensitivity linearity (typically quoted in dB) of OPD at 850 nm. (**c**) Transient photocurrent measurement for OPD. (**d**) Transient photovoltage measurement for OPD.

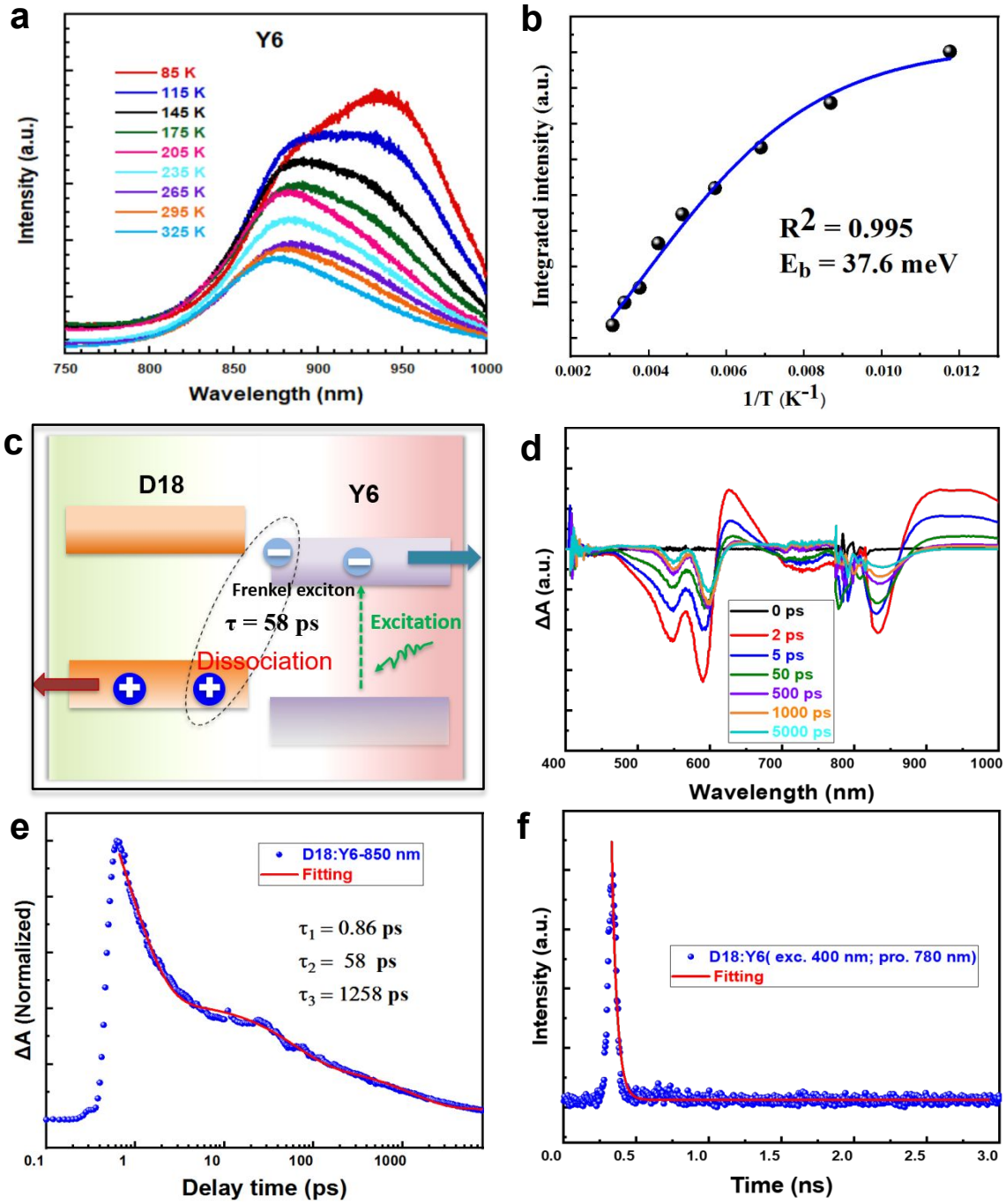

Fig. 4. (**a**) Temperature-dependent PL spectra of Y6 with rising temperature from 85 K to 325 K. (**b**) Integrated PL intensity as a function of reciprocal temperature. (**c**) Schematic state or transfer process of Frenkel excitons. (**d**) The corrected femtosecond TA spectroscopy of D18:Y6 film at selected probe delay times. (**e**) TA spectra as a function of delay time for D18:Y6 film. (**f**) The time resolved photoluminescence spectra of D18:Y6 film at probed wavelength of 780 nm.

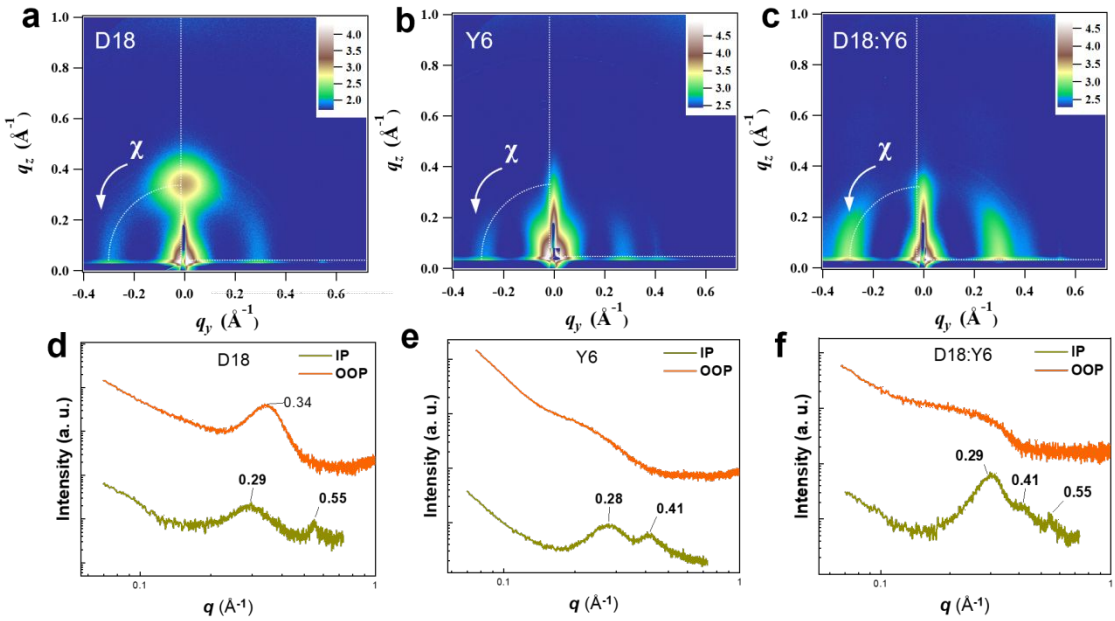

Fig. 5. 2D GISAXS pattern of neat D18 film (**a**), neat Y6 film (**b**), D18:Y6 film (**c**). 1D GISAXS profiles corresponding to 2D patterns along the IP and OOP directions for neat D18 film (**d**), neat Y6 film (**e**), D18:Y6 film (**f**).